Photoinduced Charge-Carrier Dynamics of Phototransistors Based on Perylene Diimide/Reduced Graphene Oxide Core/Shell p–n Junction Nanowires

Hojeong Yu, Piljae Joo, Dajeong Lee, Byeong-Su Kim, and Joon Hak Oh*

The tailored fabrication of multicomponent nanostructures that can exhibit superior or unique optoelectronic properties compared with those of the single-component system is highly desirable for fundamental studies of charge transport mechanisms and novel applications with advanced functions. To achieve efficient charge transport and high photoresponsivity, core/shell p–n heterojunction nanowires (NWs) are fabricated using N,N′-bis(2-phenylethyl)-perylene-3,4:9,10-tetracarboxylic diimide (BPE-PTCDI) and reduced graphene oxide (rGO) in solution phase. BPE-PTCDI/rGO core/shell NWs exhibit significantly enhanced photocurrent and faster charge compensation rate under irradiation, compared with pure BPE-PTCDI NWs. BPE-PTCDI NW core mainly acts as a light absorption layer, whereas rGO shell functions as a charge transport channel and contributes to a large electrical conductivity. Accordingly, the outstanding light-detecting performance of BPE-PTCDI/rGO NWs results from the synergistic combination of the favorable optical and electrical properties of each of the constituent materials. Intriguingly, BPE-PTCDI/rGO NW organic phototransistors (OPTs) show charge compensation behaviors opposite to those of pure BPE-PTCDI NW-OPTs, which is interpreted with a model concerning charge trapping energy levels. The results obtained herein demonstrate great promise for use of carbon-based multicomponent core/shell nanomaterials in photodetectors, and the developed methodology provides insights into the quantitative analysis of the photogenerated charge-carrier dynamics of multicomponent semiconducting systems.

1. Introduction

Organic phototransistors (OPTs) based on photoconductive organic semiconductors are promising platforms for low-cost and large-area light-detection applications, and can potentially be employed for flexible and wearable photosensors. In general, OPTs outperform conventional two-terminal organic photodiodes in terms of light-detection sensitivity and signal magnification capability, owing to the presence of an additional (i.e., third) electrode, which enables amplification of the photocurrent without inducing additional noise.[1,2]

Single-crystalline organic nanowires (NWs) have recently been used for OPTs, and nanowire OPTs (NW-OPTs) formed of intrinsically defect-free and highly ordered materials have shown great promise for miniaturizing optoelectronic devices, compared with bulk thin-film OPTs.[3–8] Most of the NW-OPTs have been fabricated from a single-component system so far,[7,9–15] and multicomponent NW systems have been far less widely used for OPTs.[16,17] Multicomponent nanoassemblies composed of single-crystalline NWs in core/shell geometry can provide a number of additional advantages compared with single-component system,[18,19] including a larger photoconductive gain, a faster photoresponse,[12] a longer charge-carrier lifetime,[16,17] and favorable exciton dissociation dynamics at the core/shell interface.[18] Therefore, the development of OPTs based on core/shell NWs is highly desirable for high-performance optoelectronic nanodevice applications as well as fundamental study on charge transport dynamics.

2D carbon materials have been used for various types of photodetectors in a broad wavelength/frequency range,[20,21] and recently employed for the fabrication of hybrid core/shell nanoassemblies,[22] such as dioctyl-PDI/rGO,[18] peptide/graphene,[23] and C$_{60}$/rGO,[19] to explore the merit of a multiplexed system. To date, however, there has been little progress on systematic study on the charge transport dynamics of organic–graphene hybrid core/shell system, coupled with characterization of their optoelectronic properties.

Here, we report multicomponent NW phototransistors based on 1D core/shell p–n heterojunction nanomaterials, which have been prepared using an n-type organic semiconductor N,N′-bis(2-phenylethyl)-perylene-3,4:9,10-tetracarboxylic diimide (BPE-PTCDI) and 2D reduced graphene oxide (rGO) as the core and shell via a simple solution mixing method. In

H. Yu, D. Lee, Prof. J. H. Oh
Department of Chemical Engineering
Pohang University of Science and
Technology (POSTECH)
Pohang, Gyeongbuk 790-784, South Korea
E-mail: joonhoh@postech.ac.kr
H. Yu, P. Joo, Prof. B.-S. Kim
Department of Chemistry & Department of
Energy Engineering
Low Dimensional Carbon Materials Center
Ulsan National Institute of Science and Technology (UNIST)
Ulsan 689-798, South Korea

ADVANCED
OPTICAL
MATERIALS
www.advopticalmat.de

Materials Views
www.MaterialsViews.com

addition, the photoinduced charge-carrier dynamics of BPE-PTCDI/rGO core/shell NWs has been thoroughly studied using quantitative analysis methods. Although pure BPE-PTCDI NW-OPTs have been found to show higher photoresponsivity and gate-field-modulated external quantum efficiency (EQE) than their thin-film counterparts in our previous study,[7] their charge-carrier mobility is still lower than that of 2D carbon nanomaterials. On the other hand, rGO typically shows the low absorption of visible light, which limits its application in photo-detectors, despite its excellent charge transport capability.[24–27] In this regard, BPE-PTCDI/rGO core/shell NWs may show enhanced optoelectronic properties, owing to the synergistic interplay of the core and shell materials. The photoinduced charge-carrier dynamics has been investigated by analyzing a number of parameters such as charge compensation rates, photoresponsivity, photoswitching ratio, and EQEs, which have been compared with those of the single-component system. In particular, the charge compensation behaviors of BPE-PTCDI/rGO NW-OPTs have been studied using a model concerning additional charge trapping energy levels. These quantitative analyses revealed that the BPE-PTCDI/rGO core/shell NWs exhibit substantially improved optoelectronic performance such as enhanced photocurrent and faster charge compensation rates, due to the synergistic effect of the optical and electrical properties of each of the constituent materials. This work demonstrates usefulness of rational design of core/shell organic nanomaterials for high-performance OPTs, and the developed methodology provides insights into the quantitative analysis of their photoinduced charge-carrier behaviors.

2. Results and Discussion

2.1. Fabrication and Characterization of BPE-PTCDI/rGO Core/Shell NWs

BPE-PTCDI NWs were fabricated using a nonsolvent nucleation method[28] and the NWs were dispersed with mild agitation in rGO solution using dimethylformamide (DMF) as the solvent (see the Experimental Section). BPE-PTCDI/rGO core/shell NWs were fabricated by utilizing van der Waals interactions between the rGO sheet and BPE-PTCDI NW. **Figure 1**a, b shows representative scanning electron microscope (SEM) images of a pure BPE-PTCDI NW and a BPE-PTCDI/rGO core/shell NW, respectively (the average diameter and length of BPE-PTCDI/rGO NWs used for device fabrication was approximately 860 ± 310 nm and 83 ± 33 μm, respectively). A typical transmission electron microscope (TEM) image of a BPE-PTCDI/rGO NW is shown in Figure 1c, and a magnified image is shown in Figure 1d, which indicates that multilayer rGO sheets were wrapped around the BPE-PTCDI NW core. Two mixing ratios (i.e., 1:1 and 2:1) of rGO sheets and BPE-PTCDI NWs were tested to obtain rGO shell with different thicknesses. The rGO shell thickness was found to be 2.2 ± 0.4 nm and 5.1 ± 0.7 nm from the mixing ratio of rGO sheet/BPE-PTCDI NW of 1:1 and 2:1, respectively (see Figure S1, Supporting Information). According to TEM analysis, this shell thickness corresponds to approximately five and ten rGO layers, respectively.

The formation of a BPE-PTCDI/rGO core/shell NW structure was further investigated by UV–vis spectroscopy. The
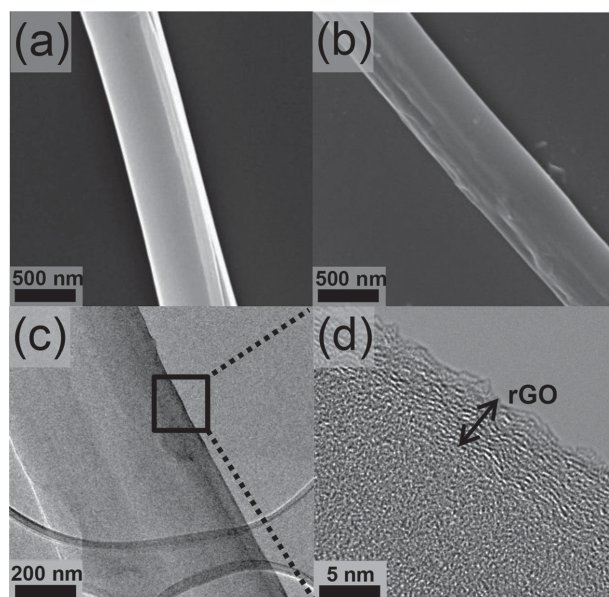

Figure 1. SEM images of a) BPE-PTCDI NW and b) BPE-PTCDI/rGO core/shell NW. c) TEM images of BPE-PTCDI/rGO core/shell NW and d) the magnified image of rGO shell.

UV–vis absorption spectra of BPE-PTCDI NWs, rGO sheets, and BPE-PTCDI/rGO NWs are shown in Figure S2 (Supporting Information). The pure rGO sheets showed the maximum band absorption at ≈260 nm, whereas the BPE-PTCDI NWs more strongly absorbed light in visible wavelengths, with absorption peaks at 325, 480, and 685 nm. In the BPE-PTCDI/rGO NW system, the maximum absorption peak arising from the BPE-PTCDI part was shifted to 560 nm, which could be attributed to the interaction between the BPE-PTCDI NW and rGO in the core/shell geometry.[29,30]

2.2. Optoelectronic Performance of BPE-PTCDI/rGO Core/Shell NWs

2.2.1. Electrical Performance of BPE-PTCDI/rGO Core/Shell NWs

To investigate optoelectronic properties of a single BPE-PTCDI/rGO NW, we fabricated NW field-effect transistors (NW-FETs) using a single rGO-wrapped BPE-PTCDI NW as the semiconducting layer on n-octadecyltrimethoxysilane (OTS)-treated SiO$_2$/Si substrates in the bottom-gate bottom-contact configuration (see the Experimental Section). **Figure 2**a shows a schematic diagram of the device structure, together with a SEM image of the device. The channel dimensions were estimated from the width (W) and length (L) of the BPE-PTCDI/rGO NW crossing the source and drain electrodes. The typical electrical performances of pure BPE-PTCDI NW, BPE-PTCDI/rGO core/shell NWs with different shell thicknesses (i.e., 2.2 and 5.1 nm) and pure rGO are presented in Figure 2b. The major charge carriers could be switched from electrons (n-channel FET) to both electrons and holes (ambipolar FET) by wrapping rGO sheets onto BPE-PTCDI NW (Figure 2c). The pristine BPE-PTCDI NWs exhibited well-defined unipolar n-channel

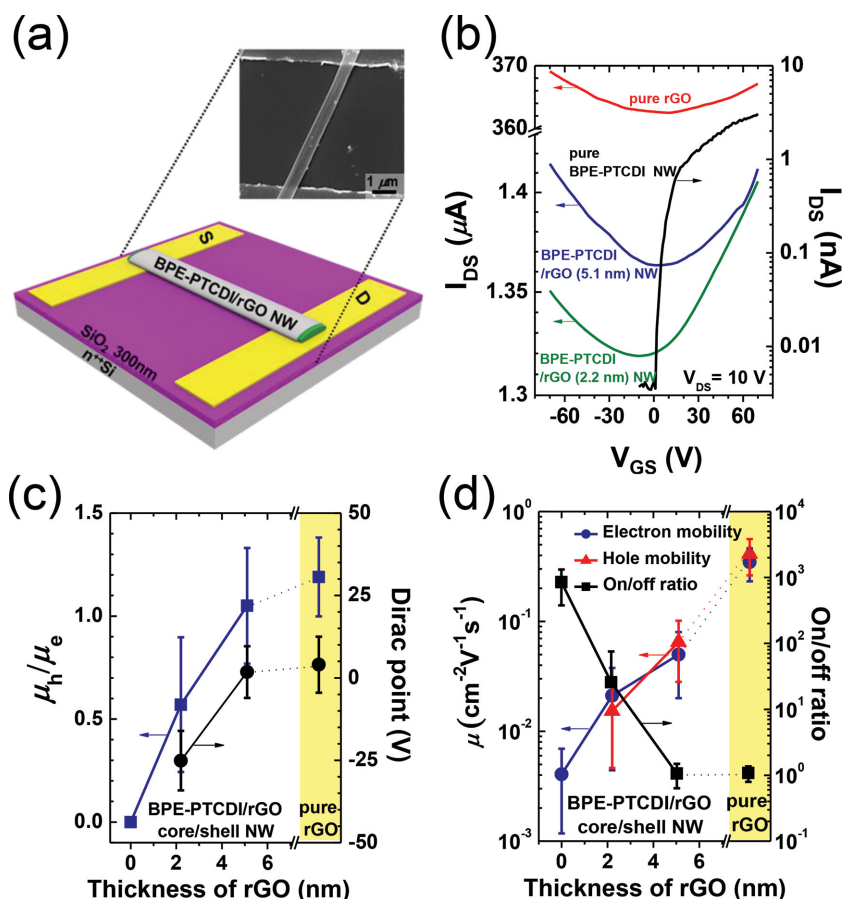www.MaterialsViews.com

ADVANCED
OPTICAL
MATERIALS
www.advopticalmat.de

FULL PAPER

Figure 2. Device structure of a) single BPE-PTCDI/rGO NW-FET and the corresponding SEM image. b) Typical *I–V* characteristics of pure BPE-PTCDI NW-FET, BPE-PTCDI/rGO core/shell NW-FETs, and pure rGO-FET in *n*-channel operation (V_{DS} = 10 V). c) Average hole and electron mobility (μ_h, μ_e) and on/off ratio variations as a function of the thickness of rGO layer. d) Average hole-to-electron mobility ratio (μ_h/μ_e) and Dirac point variations as a function of the thickness of rGO layer. The average values with the error bar of standard deviations were obtained from 10 BPE-PTCDI/rGO core/shell NW-FETs.

semiconductor (CMOS)-like inverters formed using identical BPE-PTCDI/rGO NWs as the *p*- and *n*-channel semiconductors. The NW networks were deposited via drop casting of a dispersed BPE-PTCDI/rGO NW solution, covering interdigitated gold source and drain electrodes. A schematic diagram of the CMOS-like inverter is shown in Figure S3a (Supporting Information). A common *n*-doped Si gate functions as the input voltage V_{IN}, while the *p*-FET is grounded as the driver and the *n*-FET functions as the load transistor and provides a supply voltage of V_{DD} = −10 V. The voltage inversion was obtained with a maximum gain of 1.1 (see Figure S3b, Supporting Information). This is comparable to that of other graphene-based inverters.[35,36]

2.2.2. Photoswitching Characteristics of BPE-PTCDI/rGO Core/Shell NW-OPTs

To investigate the optoelectronic properties of single BPE-PTCDI/rGO NWs, the photoresponse of the BPE-PTCDI/rGO NW-OPTs upon on-and-off switching of polychromatic light (λ = 450–650 nm, λ_{max} = 640 nm, P_{max} = 36 mW cm^{-2}) was monitored. Note that the maximum absorption wavelength of the BPE-PTCDI/rGO NWs ($\lambda_{abs, max}$ = 560 nm) was closely matched with the spectrum of the polychromatic light, compared with pure rGO sheets ($\lambda_{abs, max}$ = 260 nm) and pure BPE-PTCDI NWs ($\lambda_{abs, max}$ = 685 nm). Furthermore, our control experiment using rGO sheets revealed that the rGO sheets themselves were not responsive to illumination (see Figures S4 and S5, Supporting

performance. When the thickness of rGO shell was ≈2.2 nm (≈5 rGO layers), electron-dominant ambipolar charge transport was observed, indicating that the core *n*-channel BPE-PTCDI NW could clearly act as the channel layer. As the thickness of rGO sheet was increased up to ≈5.1 nm (≈10 rGO layers), slightly hole-dominant ambipolar property, but with an average hole-to-electron mobility ratio (μ_h/μ_e) nearly identical to ≈1 and an average Dirac point of ≈0 V (Figure 2d), was observed due to the enhanced effect of the electrical properties of the rGO shell as the channel. However, the average ratio of hole and electron mobilities of BPE-PTCDI NW/rGO core/shell NWs was still slightly lower than that of pure rGO. This indicates that BPE-PTCDI core may still affect the channel region. In addition, the on/off ratio decreased rapidly as the rGO shell thickness increased. It is common to observe such a low on/off ratio from graphene-based FET devices, because of the absence of bandgap in graphene.[31,32] The electrical behaviors of pure rGO-FETs obtained from our control experiment were in good agreement with those of other rGO-based FETs reported previously.[33,34]

Their well-balanced ambipolar transport properties may extend their applications to complementary metal-oxide

Information).

Interestingly, the photogenerated charge carriers in the BPE-PTCDI/rGO NW exhibited opposite trends to those of pure BPE-PTCDI NW-OPTs,[7] as shown in **Figure 3**a,b. The BPE-PTCDI/rGO NWs exhibited depletion behaviors under irradiation with visible light and accumulation behaviors upon turning off the light. Such photocurrent decay behavior under illumination has so far not been thoroughly investigated and even not been frequently observed in multicomponent organic semiconductor system. Similar photocurrent quenching was observed from single-component inorganic semiconductors, due to the metastable electronic states in the bandgap.[37] A continuous decrease in the photocurrent was observed as a function of the illumination time, which suggests the existence of metastable states that can be occupied by photoelectrons. Huang et al.[38] suggested the existence of accepter levels (i.e., a recombination center and a hole trap center) in an inorganic photoconductor, which leads to photocurrent quenching due to the absorption of light with a photon energy smaller than the bandgap.

In this regard, these photocurrent quenching phenomena of the BPE-PTCDI/rGO NWs may result from a number of factors
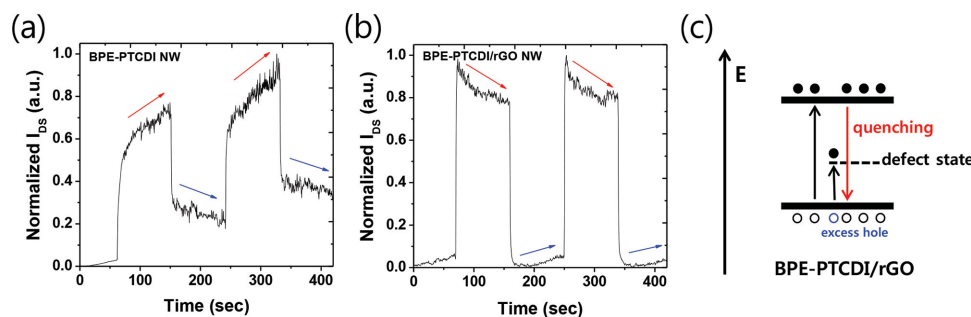
Figure 3. Photocurrent responses upon on-and-off switching of the irradiation (polychromatic light, 36 mW cm^{-2}) as a function of time for a) BPE-PTCDI NW-OPT and b) BPE-PTCDI/rGO core/shell NW-OPT at transistor off-state; $V_{GS} = 0$ V, $|V_{DS}| = 100$ V c) Model for photocurrent quenching; excess holes created by electrons excited to the defect state may facilitate the recombination of photogenerated charge carriers, leading to a decrease in photocurrent.

based on the existence of accepter levels in the core/shell system (note that there were no photocurrent quenching phenomena in pure BPE-PTCDI[7] and rGO sheets[39]: 1) The formation of a depletion heterojunction layer due to the difference in the energy levels can lead to a gradual decrease in current with illumination time by capturing photogenerated charge carriers. Holes in the depletion layer can recombine with photogenerated electrons induced at the core NW. 2) Surface defects and/or interfacial traps in the core/shell geometry and/or in the active layer/dielectric interface introduce additional charge trapping energy levels in the bandgap.[40,41] Holes can recombine with free electrons, leading to a decrease in electron density, as described by the photocurrent quenching model, shown in Figure 3c. When the illumination is switched off, the number of excess holes decreases over time and leads to an increase in the photocurrent due to the reduction in the recombination rate. 3) Rapid photocurrent saturation via the rGO shell can also lead to photocurrent quenching after the illumination is turned on.

2.2.3. Charge-Carrier Dynamics of BPE-PTCDI/ rGO Core/Shell NW-OPTs

For a quantitative analysis, time response of the BPE-PTCDI/rGO NW-OPTs to the pulsed incident light at the transistor off-state ($V_{GS} = 0$ V and $V_{DS} = 100$ V for n-channel operation, and $V_{GS} = 0$ V and $V_{DS} = -100$ V for p-channel operation) and at the transistor on-state ($V_{GS} = 100$ V and $V_{DS} = 100$ V for n-channel operation, and $V_{GS} = -100$ V and $V_{DS} = -100$ V for p-channel operation) were investigated (see **Figure 4**a, b for the transistor off-state). Under illumination, the photogenerated charge carriers in the NW core can significantly increase the charge density in the rGO layer, as can be seen from the enhanced photocurrent of the core/shell NW (Figure S6, Supporting Information). The BPE-PTCDI/rGO NW-OPTs
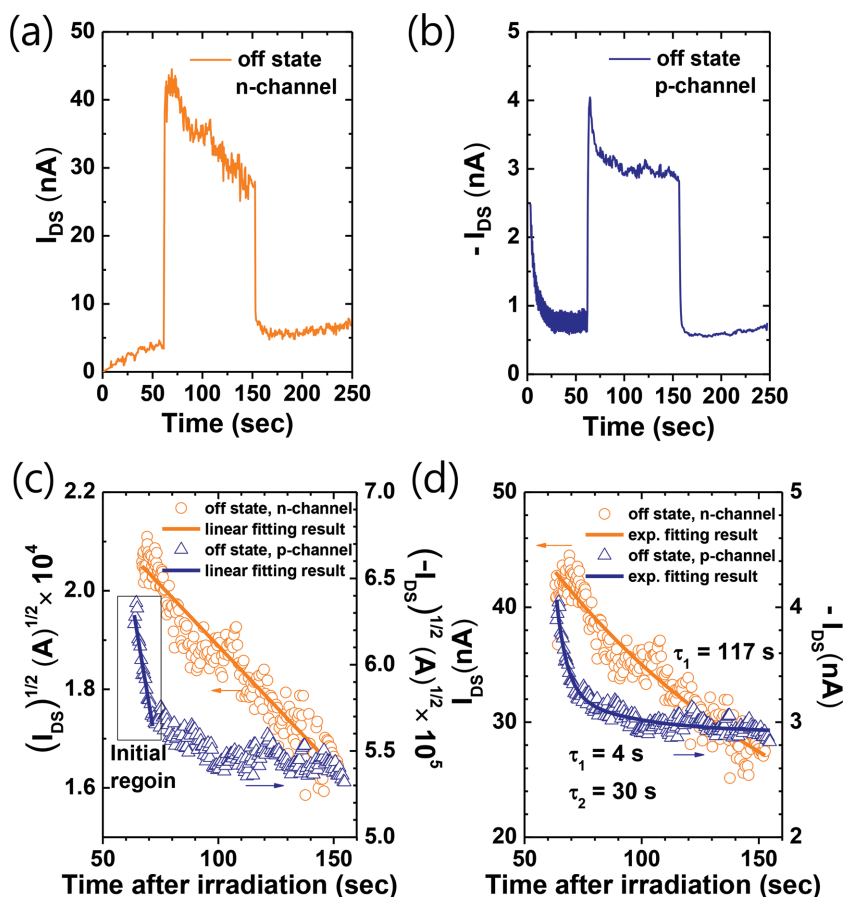
exhibited higher off-state photocurrents compared with several nanoampere-scale off-currents of pure BPE-PTCDI NW-OPTs in n-channel operation,[7] which is attributed to the enhanced charge transport properties of the π-conjugated network of the rGO shell.[18] Typically, single-layer graphene has a picosecond photocarrier lifetime, with ultrafast charge recombination,[16] and the absorption of visible light in rGO sheets is much lower

Figure 4. Time response of the BPE-PTCDI/rGO NW-OPTs to the pulsed incidence light (polychromatic light, 36 mW cm^{-2}), measured at transistor off-state; a) $V_{GS} = 0$ V, $V_{DS} = 100$ V for n-channel operation b) $V_{GS} = 0$ V, $V_{DS} = -100$ V for p-channel operation c) Charge depletion rate calculations using Equation (1) and a least-squares linear fit. d) Time response calculations of photocurrent quenching process using Equation (2), (3) and an exponential fit.

than BPE-PTCDI (see Figure S2, Supporting Information). Therefore, we can conclude that the rGO layers in our system function as a charge transport channel and contribute to a large electrical conductivity rather than an absorption layer. Accordingly, the BPE-PTCDI/rGO NWs can be utilized as a photoresponsive material in OPTs, combining the favorable optical and electrical performance of each of the constituent materials.

The initial photoresponses of BPE-PTCDI/rGO NW upon light on-and-off switching were extracted to calculate the charge depletion/accumulation rates using Equation (1):[7]

$$\text{rate} = \frac{dQ}{dt} = C\frac{dV_{\text{T}}(t)}{dt} = -\left[\frac{2LC}{\mu_{\text{sat}}W}\right]^{1/2}\frac{d\left(I_{\text{D}}(t)\right)^{1/2}}{dt} \quad (1)$$

The reduction in the photocurrent with time after turning on the light source is related to rapid recombination of photogenerated charge carriers in the depletion region. The depletion rates in the BPE-PTCDI/rGO NW-OPT were found to be 1.31×10^{10} cm^{-2} s^{-1} under n-channel operation (see the round symbols with the linear fit shown in Figure 4c) and 3.61×10^{11} cm^{-2} s^{-1} under p-channel operation (see the initial stage of triangular symbols and the linear fit shown in Figure 4c) in the transistor off-state. The photocurrent under illumination decreased in one step under n-channel operation, whereas there were two steps in p-channel operation, with an initial rapid charge decay process and a secondary slower decay process. The charge decay curves of the photocurrents in the transistor off-state can be described by

$$I(t) = I_{\text{dark}} + A\left[\exp\left(-t/\tau_1\right)\right] \quad (2)$$

$$I(t) = I_{\text{dark}} + A\left[\exp\left(-t/\tau_1\right)\right] + B\left[\exp\left(-t/\tau_2\right)\right] \quad (3)$$

where t is time, τ_1 and τ_2 are time constants, I_{dark} is the dark current, and A and B are scaling constants. Fitting the experimental data showed that the charge quenching time of the photocurrent under n-channel operation followed the monoexponential decay behavior of Equation (2), whereas that of the photocurrent in p-channel operation followed the second-order exponential decay function in Equation (3). In the transistor off-state, the charge quenching time constant was $\tau_1 = 117$ s for n-channel operation. In p-channel operation, the initial charge quenching step of the photocurrent was $\tau_1 = 4$ s and the secondary charge quenching time constant was $\tau_2 = 30$ s, as shown in Figure 4d. Note that the photocurrent under n-channel operation was an order of magnitude higher than that under p-channel operation. Under n-channel bias conditions, electron transport occurs via both the rGO shell and the n-channel of the BPE-PTCDI core; however, under p-channel bias conditions, holes cannot be transported in the n-channel core and instead undergo more rapid initial quenching. Such the second-order photocurrent decay has also been reported in rGO-based phototransistors under p-channel bias conditions.[10,42]

After the light source was turned off, charge carriers were accumulated with the rate of 3.12×10^9 cm^{-2} s^{-1} in the n-channel region and 1.45×10^{10} cm^{-2} s^{-1} in the p-channel region (see Figure S7, Supporting Information). The increase in the photo-

current with time after switch-off indicates that the recombination rate decreased. According to the charge-carrier dynamics described in our previous research,[7] pure BPE-PTCDI NW-OPTs showed an accumulation rate of 2.76×10^9 cm^{-2} s^{-1} under illumination and a recombination rate of 1.17×10^9 cm^{-2} s^{-1} after the light source was turned off. It turns out that BPE-PTCDI/rGO NWs exhibit faster charge compensation rates (charge depletion/accumulation rates) upon light on-and-off switching, compared with those (charge accumulation/release rates) of the pure BPE-PTCDI NW-OPTs.

2.2.4. Photosensitivity of BPE-PTCDI/rGO Core/Shell NW-OPTs

We investigated the responsivity R and photocurrent/dark-current ratio P and compared the photosensitivity with that of pure BPE-PTCDI NW-OPT. R and P is defined by the following equations:[5]

$$R = \frac{I_{\text{ph}}}{P_{\text{inc}}} = \frac{\left(I_{\text{light}} - I_{\text{dark}}\right)}{P_{\text{inc}}} \quad (4)$$

$$P = \frac{\left(I_{\text{light}} - I_{\text{dark}}\right)}{I_{\text{dark}}} \quad (5)$$

where I_{ph} is the photocurrent, P_{inc} is the incident illumination power, I_{light} is the drain current under illumination, and I_{dark} is the drain current in the dark. The values of R and P for the pure BPE-PTCDI NW-OPTs and BPE-PTCDI/rGO NW-OPTs are plotted as a function of V_{DS} in **Figure 5**. We observed a maximum of $R = 5.63$ AW^{-1} for the BPE-PTCDI/rGO NW-OPTs under n-channel operation (for the pure BPE-PTCDI NW-OPTs, we observed $R = 3.97$ AW^{-1}). The enhancement of the responsivity is due to the synergistic interaction of the efficient exciton dissociation[18] and more rapid charge transport via the rGO shell.[16,18] On the other hand, similar maximum values of P were obtained from both the pure BPE-PTCDI NW-OPT ($P = 17.6$) and rGO/BPE-PTCDI NW-OPT devices ($P = 17.5$). R was strongly affected by the presence of the rGO shell, whereas P was not affected by the shell material. This is in line with our previous findings that R is closely related to the intrinsic optical properties of photoconducting materials, whereas P is more dependent on the incident optical power density.[7]

The EQE (η) of the single BPE-PTCDI/rGO NW can be calculated using the following expression:[43]

$$\eta = \frac{\left(I_{\text{light}} - I_{\text{dark}}\right)hc}{eP_{\text{inc}}A\lambda_{\text{peak}}} \quad (6)$$

where h is the Plank constant, c the speed of light, e the fundamental unit of charge, A the area of the transistor channel and λ_{peak} the peak wavelength of the incident light. **Figure 6** shows the EQE for the BPE-PTCDI/rGO NW-OPTs and pure BPE-PTCDI NW-OPTs as a function of V_{DS} (with $V_{\text{GS}} = 0$ V) under n-channel operation. The BPE-PTCDI/rGO NW-OPTs exhibited a relatively large EQE of $\eta = 1090\%$, whereas the pure BPE-PTCDI NW-OPTs exhibited $\eta = 679\%$ under the same
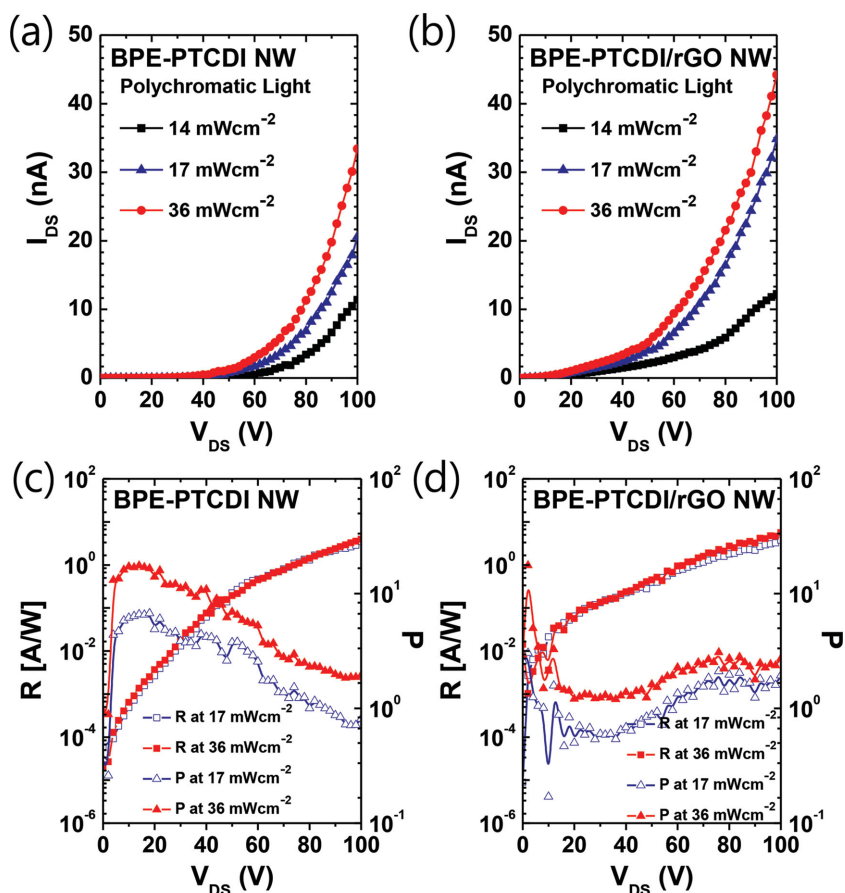
FULL PAPER

Figure 5. $I_{DS}-V_{DS}$ curves at $V_{GS} = 0$ V and $V_{DS} = 100$ V measured over a) BPE-PTCDI NW-OPT and b) BPE-PTCDI/rGO core/shell NW-OPT in the dark and under polychromatic light irradiation of increasing power density. Responsivity (R) and photocurrent/dark-current ratio (P) of c) BPE-PTCDI NW-OPT and d) BPE-PTCDI/rGO core/shell NW-OPT.
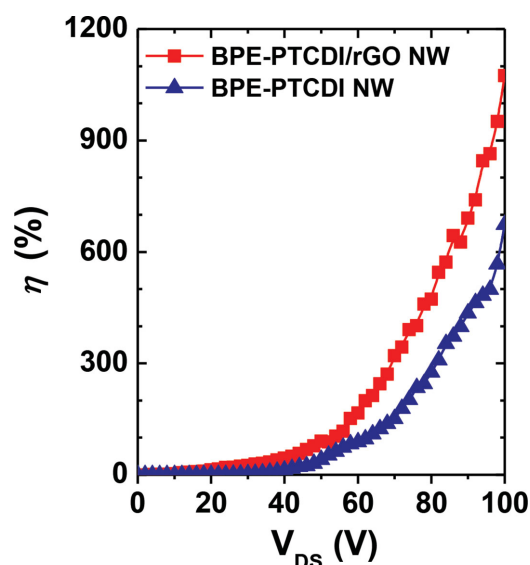

Figure 6. External quantum efficiency (EQE; η) as a function of V_{DS} of a) pure BPE-PTCDI NW-OPT and b) BPE-PTCDI/rGO NW-OPT under polychromatic light with irradiation power of 17 mW cm^{-2} at $V_{GS} = 0$ V and $V_{DS} = 100$ V.

optical power density of $P_{inc} = 17$ mW cm^{-2}. The BPE-PTCDI/rGO NW-OPTs can generate more photoelectrons than the pure BPE-PTCDI NW-OPTs, achieving lower power consumption. The EQE greater than 100% for the photoactive BPE-PTCDI/rGO NW device indicates that the photomultiplication effectively takes place.[44] Such enhancement in all the optoelectrical parameters clearly demonstrates the synergistic effect of BPE-PTCDI/rGO core/shell NW geometry.

3. Conclusion

We have synthesized BPE-PTCDI/rGO NWs in the solution phase by exploiting conventional van der Waals interactions. While BPE-PTCDI NW core mainly acts as light absorption layer, rGO shell functions as a charge transport layer and contributes to large electrical conductivity. The BPE-PTCDI/rGO NWs could also be utilized as ambipolar semiconductors for the implementation of CMOS-like inverters. Owing to the synergistic interplay of the optical and electrical properties of the core and shell materials, the charge compensation rate of the BPE-PTCDI/rGO NW-OPT device was three to five times higher upon light on-and-off switching and the EQE of the BPE-PTCDI/rGO NW-OPT device was approximately two times larger than those of the pure BPE-PTCDI NW-OPT. Interestingly, BPE-PTCDI/rGO NW-OPTs showed charge compensation behaviors opposite to those of pure BPE-PTCDI NW-OPTs. This phenomenon was discussed in terms of the existence of charge trapping energy levels. The work described here represents an approach to obtaining p–n heterojunction multicomponent nanomaterials and describes the quantitative analysis on the charge transport behaviors, which will enable the development of optoelectronic devices that exhibits ambipolar charge transport behavior, a high photoresponsivity, and multiplication of the photocurrent.

4. Experimental Section

Preparation of BPE-PTCDI/rGO Core/Shell NWs: BPE-PTCDI NWs were fabricated with a nonsolvent nucleation method as reported previously.[28] Graphene oxide (GO) was prepared with a modified Hummers method,[45,46] and chemically reduced in DMF solvent as reported previously.[47] BPE-PTCDI NWs were dispersed with mild agitation in rGO solution (0.3 mg mL^{-1}) for 15 min, followed by centrifugation at 3000 rpm. The mixing ratio of dispersed rGO sheets and BPE-PTCDI NWs was varied as 1:1 and 2:1, respectively. Freestanding remnant rGO sheets were removed three times. The precipitated BPE-PTCDI/rGO core/shell NWs were washed thoroughly with DMF solvent, and redispersed in a clean DMF solvent.

www.MaterialsViews.com

ADVANCED
OPTICAL
MATERIALS
www.advopticalmat.de

FULL PAPER

Fabrication and Characterization of BPE-PTCDI/rGO NW-OPTs: A heavily *n*-doped Si wafer with a thermally grown 300-nm-thick SiO$_2$ layer ($C_i = 10$ nF cm^{-2}) was used as the gate and the dielectric layer, respectively. The bottom-contact electrodes were defined *via* conventional photolithography on top of SiO$_2$/Si wafers, and the SiO$_2$/Si wafer was modified by treating with *n*-OTS vaporized at 110 °C for 12 h. The BPE-PTCDI/rGO NW dispersions were drop-cast on the prepared substrates to fabricate bottom-contact BPE-PTCDI/rGO NW-OPTs. The current–voltage (*I–V*) characteristics of the devices were measured in N$_2$ atmosphere by using a Keithley 4200-SCS semiconductor parameter analyzer.

Supporting Information

Supporting Information is available from the Wiley Online Library or from the author.

Acknowledgements

[1] *Optoelectronic Sensors*, Vol. *1* (Ed: J. H. D. Decoster), Wiley-ISTE, London **2009**.

[2] *Physics of Semiconductor Devices*, Vol. *3*, (Ed: K. K. N. S. M. Sze), John Wiley & Sons, Hoboken, NJ, USA **2007**.

[3] Q. X. Tang, L. Q. Li, Y. B. Song, Y. L. Liu, H. X. Li, W. Xu, Y. Q. Liu, W. P. Hu, D. B. Zhu, *Adv. Mater.* **2007**, *19*, 2624.

[4] K. H. Kim, S. Y. Bae, Y. S. Kim, J. A. Hur, M. H. Hoang, T. W. Lee, M. J. Cho, Y. Kim, M. Kim, J. I. Jin, S. J. Kim, K. Lee, S. J. Lee, D. H. Choi, *Adv. Mater.* **2011**, *23*, 3095.

[5] Y. L. Guo, C. Y. Du, G. Yu, C. A. Di, S. D. Jiang, H. X. Xi, J. Zheng, S. K. Yan, C. L. Yu, W. P. Hu, Y. Q. Liu, *Adv. Funct. Mater.* **2010**, *20*, 1019.

[6] A. L. Briseno, S. C. B. Mannsfeld, S. A. Jenekhe, Z. Bao, Y. N. Xia, *Mater. Today* **2008**, *11*, 38.

[7] H. Yu, Z. Bao, J. H. Oh, *Adv. Funct. Mater.* **2013**, *23*, 629.

[8] Z. H. Sun, J. H. Li, F. Yan, *J. Mater. Chem.* **2012**, *22*, 21673.

[9] Y. Che, X. Yang, G. Liu, C. Yu, H. Ji, J. Zuo, J. Zhao, L. Zang, *J. Am. Chem. Soc.* **2010**, *132*, 5743.

[10] B. Chitara, L. S. Panchakarla, S. B. Krupanidhi, C. N. Rao, *Adv. Mater.* **2011**, *23*, 5419.

[11] H. Kind, H. Q. Yan, B. Messer, M. Law, P. D. Yang, *Adv. Mater.* **2002**, *14*, 158.

[12] J. S. Jie, W. J. Zhang, Y. Jiang, X. M. Meng, Y. Q. Li, S. T. Lee, *Nano Lett.* **2006**, *6*, 1887.

[13] R. Calarco, M. Marso, T. Richter, A. I. Aykanat, R. Meijers, V. D. H. A, T. Stoica, H. Luth, *Nano Lett.* **2005**, *5*, 981.

[14] K. J. Baeg, M. Binda, D. Natali, M. Caironi, Y. Y. Noh, *Adv. Mater.* **2013**, *25*, 4267.

[15] M. El Gemayel, M. Treier, C. Musumeci, C. Li, K. Mullen, P. Samori, *J. Am. Chem. Soc.* **2012**, *134*, 2429.

[16] H. Lee, K. Heo, J. Park, Y. Park, S. Noh, K. S. Kim, C. Lee, B. H. Hong, J. Jian, S. Hong, *J. Mater. Chem.* **2012**, *22*, 8372.

[17] X. W. Fu, Z. M. Liao, Y. B. Zhou, H. C. Wu, Y. Q. Bie, J. Xu, D. P. Yu, *Appl. Phys. Lett.* **2012**, *100*, 223114.

[18] S. Wang, B. M. Goh, K. K. Manga, Q. Bao, P. Yang, K. P. Loh, *ACS Nano* **2010**, *4*, 6180.

[19] J. Yang, M. Heo, H. J. Lee, S. M. Park, J. Y. Kim, H. S. Shin, *ACS Nano* **2011**, *5*, 8365.

[20] J. H. Li, L. Y. Niu, Z. J. Zheng, F. Yan, *Adv. Mater.* **2014**, *26*, 5239.

[21] H. X. Chang, Z. H. Sun, M. Saito, Q. H. Yuan, H. Zhang, J. H. Li, Z. C. Wang, T. Fujita, F. Ding, Z. J. Zheng, F. Yan, H. K. Wu, M. W. Chen, Y. Ikuhara, *ACS Nano* **2013**, *7*, 6310.

[22] D. Y. Yoo, N. D. K. Tu, S. L. Lee, E. Lee, S. R. Jeon, S. Hwang, H. S. Lim, J. K. Kim, B. K. Ju, H. Kim, J. A. Lim, *ACS Nano* **2014**, *8*, 4248.

[23] T. H. Han, W. J. Lee, D. H. Lee, J. E. Kim, E. Y. Choi, S. O. Kim, *Adv. Mater.* **2010**, *22*, 2060.

[24] G. Eda, G. Fanchini, M. Chhowalla, *Nat. Nanotechnol.* **2008**, *3*, 270.

[25] H. Hwang, P. Joo, M. S. Kang, G. Ahn, J. T. Han, B. S. Kim, J. H. Cho, *ACS Nano* **2012**, *6*, 2432.

[26] I. Jung, D. A. Dikin, R. D. Piner, R. S. Ruoff, *Nano Lett.* **2008**, *8*, 4283.

[27] X. Liu, E. K. Lee, J. H. Oh, *Small* **2014**, *10*, 3700.

[28] J. H. Oh, H. W. Lee, S. Mannsfeld, R. M. Stoltenberg, E. Jung, Y. W. Jin, J. M. Kim, J. B. Yoo, Z. Bao, *Proc. Natl. Acad. Sci. USA* **2009**, *106*, 6065.

[29] A. Chunder, T. Pal, S. I. Khondaker, L. Zhai, *J. Phys. Chem. C* **2010**, *114*, 15129.

[30] R. A. Hatton, N. P. Blanchard, V. Stolojan, A. J. Miller, S. R. P. Silva, *Langmuir* **2007**, *23*, 6424.

[31] B. J. Kim, H. Jang, S. K. Lee, B. H. Hong, J. H. Ahn, J. H. Cho, *Nano Lett.* **2010**, *10*, 3464.

[32] C. Gomez-Navarro, R. T. Weitz, A. M. Bittner, M. Scolari, A. Mews, M. Burghard, K. Kern, *Nano Lett.* **2007**, *7*, 3499.

[33] X. Li, H. Wang, J. T. Robinson, H. Sanchez, G. Diankov, H. Dai, *J. Am. Chem. Soc.* **2009**, *131*, 15939.

[34] G. Eda, G. Fanchini, M. Chhowalla, *Nat. Nanotechnol.* **2008**, *3*, 270.

[35] F. Traversi, V. Russo, R. Sordan, *Appl. Phys. Lett.* **2009**, *94*, 223312.

[36] C. Hong-Yan, J. Appenzeller, presented at *69th Annual Device Research Conference (DRC 2011)*, Santa Barbara, CA, 20-22 June **2011**.

[37] S. J. Chung, M. S. Jeong, O. H. Cha, C. H. Hong, E. K. Suh, H. J. Lee, Y. S. Kim, B. H. Kim, *Appl. Phys. Lett.* **2000**, *76*, 1021.

[38] Z. C. Huang, D. B. Mott, P. K. Shu, R. Zhang, J. C. Chen, D. K. Wickenden, *J. Appl. Phys.* **1997**, *82*, 2707.

[39] S. Safa, R. Sarraf-Mamoory, R. Azimirad, *Physica E* **2014**, *57*, 155.

[40] W. K. Hong, J. I. Sohn, D. K. Hwang, S. S. Kwon, G. Jo, S. Song, S. M. Kim, H. J. Ko, S. J. Park, M. E. Welland, T. Lee, *Nano Lett.* **2008**, *8*, 950.

[41] F. Gu, P. Wang, H. Yu, B. Guo, L. Tong, *Opt. Express* **2011**, *19*, 10880.

[42] G. Konstantatos, M. Badioli, L. Gaudreau, J. Osmond, M. Bernechea, F. Pelayo Garcia de Arquer, F. Gatti, F. H. L. Koppens, *Nat. Nanotechnol.* **2012**, *7*, 363.

[43] J. G. Labram, P. H. Wöbkenberg, D. D. C. Bradley, T. D. Anthopoulos, *Org. Electron.* **2010**, *11*, 1250.

[44] M. Hiramoto, T. Imahigashi, M. Yokoyama, *Appl. Phys. Lett.* **1994**, *64*, 187.

[45] W. S. Hummers, R. E. Offeman, *J. Am. Chem. Soc.* **1958**, *80*, 1339.

[46] N. I. Kovtyukhova, P. J. Ollivier, B. R. Martin, T. E. Mallouk, S. A. Chizhik, E. V. Buzaneva, A. D. Gorchinskiy, *Chem. Mater.* **1999**, *11*, 771.

[47] S. Park, J. An, I. Jung, R. D. Piner, S. J. An, X. Li, A. Velamakanni, R. S. Ruoff, *Nano Lett.* **2009**, *9*, 1593.